

EnvGS: Modeling View-Dependent Appearance with Environment Gaussian

Tao Xie^{1*} Xi Chen^{1*} Zhen Xu¹ Yiman Xie¹ Yudong Jin¹
 Yujun Shen² Sida Peng¹ Hujun Bao¹ Xiaowei Zhou¹

¹ Zhejiang University ² Ant Group

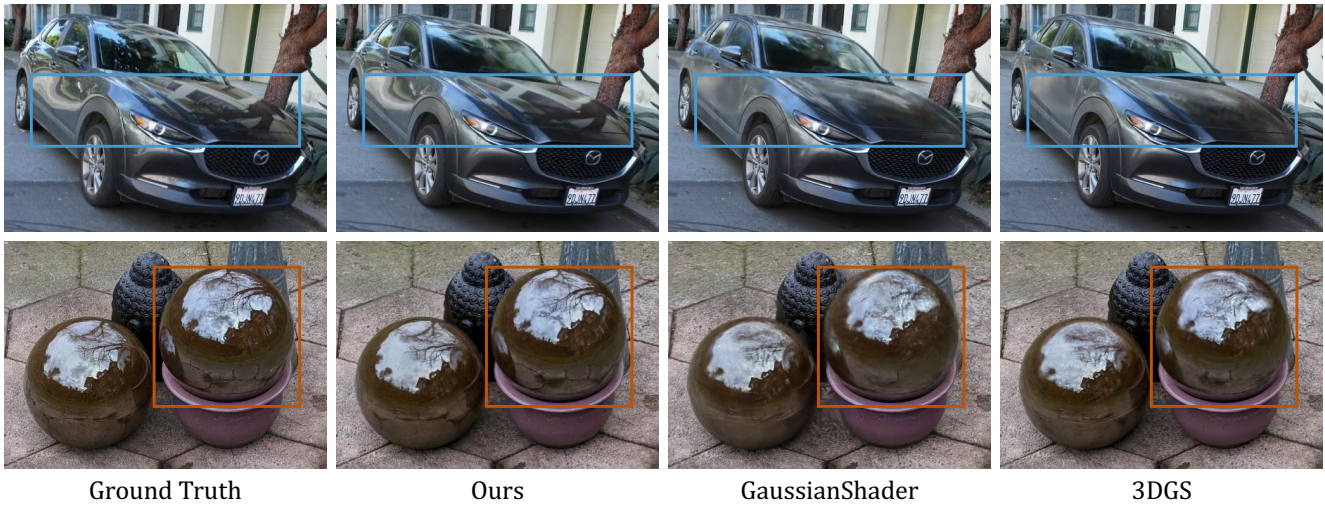


Figure 1. **Photorealistic, real-time rendering of real-world scenes with complex reflections.** Our proposed EnvGS outperforms prior works in capturing complex reflection effects, especially near-field reflections and high-frequency details while maintaining real-time rendering speed. Please see our supplementary video for better visualizations.

Abstract

Reconstructing complex reflections in real-world scenes from 2D images is essential for achieving photorealistic novel view synthesis. Existing methods that utilize environment maps to model reflections from distant lighting often struggle with high-frequency reflection details and fail to account for near-field reflections. In this work, we introduce EnvGS, a novel approach that employs a set of Gaussian primitives as an explicit 3D representation for capturing reflections of environments. These environment Gaussian primitives are incorporated with base Gaussian primitives to model the appearance of the whole scene. To efficiently render these environment Gaussian primitives, we developed a ray-tracing-based renderer that leverages the GPU’s RT core for fast rendering. This allows us to jointly optimize our model for high-quality reconstruction while maintain-

ing real-time rendering speeds. Results from multiple real-world and synthetic datasets demonstrate that our method produces significantly more detailed reflections, achieving the best rendering quality in real-time novel view synthesis. The code is available at <https://zju3dv.github.io/envgs>.

1. Introduction

Novel view synthesis aims to generate novel views of 3D scenes based on a set of input images, which enables many applications such as VR/AR, and autonomous driving. Recent advances in Neural Radiance Fields (NeRF) [24] have demonstrated impressive rendering performance. However, NeRF’s high computational cost makes it challenging for real-time applications. More recently, 3D Gaussian Splatting (3DGS) [15] explicitly models scenes with 3D Gaussian primitives and utilizes rasterization for rendering, achieving real-time rendering with competitive quality. However, modeling complex high-frequency specular

* Equal Contribution.

reflections remains challenging for 3DGS due to the limited expressiveness of the Spherical Harmonics (SH).

Recent works GaussianShader [13] and 3DGS-DR [43], enhance 3DGS by integrating an environment map and employing shading functions to blend the appearance from both the environment map and SH for the final rendering. While additional environmental lighting can enhance 3DGS’s reflection modeling ability, it still struggles to reconstruct complex specular reflections accurately due to two factors. First, the assumption of distant lighting in environment maps limits their ability to only capture distant illumination and difficult to synthesize accurate near-field reflections. Second, this representation inherently lacks sufficient capacity to capture high-frequency reflection details.

In this paper, we present EnvGS, a novel approach for modeling complex reflections in real-world scenes, addressing the aforementioned challenges. We propose to model reflections using a set of Gaussian primitives termed the *environment Gaussian*. The geometry and base appearance are represented by another set of Gaussian primitives called *base Gaussian*. We effectively blend the two Gaussians for rendering and optimization. Our rendering process begins with rendering the *base Gaussian* for the per-pixel surface position, normal, base color, and blending weight. Next, we render the *environment Gaussian* at the surface point in the direction of the reflection of the viewing direction around the surface normal to capture reflection colors. Finally, we blend the base color with the reflection color to achieve the final rendering results. In contrast to previous methods, EnvGS captures high-frequency reflection details using Gaussian primitives, offering superior modeling capabilities compared to environment maps. Additionally, our explicit 3D reflection representation eliminates the need for distant lighting assumptions, enabling accurate modeling of near-field reflections, as shown in Fig. 1.

To render the *environment Gaussian* at each intersection point along the reflection direction, we create a fully differentiable ray-tracing renderer for 2DGS since rasterization is not suited for this task. We build the ray-tracing renderer on CUDA and OptiX [27] for real-time rendering and efficient optimization of *environment Gaussian*. The rendering process starts by constructing a bounding volume hierarchy (BVH) from the 2D Gaussian primitives. We then cast rays against the BVH, gathering ordered intersections in chunks while integrating the Gaussian properties through volume rendering [14] to achieve the final results. Our Gaussian ray-tracing renderer enables detailed reflection rendering at real-time performance. Furthermore, it allows for efficient joint optimization of the *environment Gaussian* and *base Gaussian*, which is essential for accurate reflection modeling, as demonstrated in Sec 5.4.

To validate the effectiveness of our method, we evaluate EnvGS on several real and synthetic datasets. The re-

sults demonstrate that our methods achieve state-of-the-art performance in real-time novel view synthesis and considerably surpass existing real-time methods, particularly in synthesizing complex reflections in real-world scenes.

In summary, we make the following contributions:

- We propose a novel scene representation for accurately modeling complex near-field and high-frequency reflections in real-world environments.
- We developed a real-time ray-tracing renderer for 2DGS, enabling joint optimization of our representation for accurate scene reconstruction while achieving real-time rendering speeds.
- Extensive experiments shows that EnvGS significantly outperforms previous methods. To the best of our knowledge, EnvGS is the first method that achieves real-time photorealistic specular reflections synthesizing in real-world scenes.

2. Related Work

Our work falls into the area of learning scene representations from a set of posed RGB images. In this section, we review both NeRF-based and Gaussian Splatting-based representations, with a focus on how these methods handle view-dependent effects.

Neural Radiance Field. NeRF [24] introduced the concept of neural radiance fields, which model scenes as implicit multilayer perceptrons (MLPs) and render them via volume rendering, achieving impressive results in novel view synthesis. Subsequent advancements focused on enhancing rendering quality [2–4] and computational efficiency. [6, 7, 20, 26, 31]. [18, 36, 37, 41] introduce Signed Distance Field into NeRF to improve geometry quality. However, these methods often model view-dependent effects via simple viewing directions, which can lead to blurry reflection renderings. To address this, Ref-NeRF [33] encodes the outgoing radiance using the reflected view direction, yielding improved results under distant lighting conditions. Follow-up works [8, 19, 21, 35] leverage Signed Distance Fields (SDF) to refine surface normals to enhance reflection and geometry quality. SpecNeRF [23] further incorporates spatially varying Gaussian directional encoding to better capture near-field reflections. NeRF-Casting [34] represents the scene in a unified manner, similar to [4], and performs ray marching along reflection directions to integrate reflection features, which are then decoded into color with MLPs. This approach achieves impressive results on real-world data under both near and distant lighting conditions. However, the requirement for multiple MLP queries per ray makes NeRF-Casting unsuitable for real-time rendering and necessitates substantial training time. In contrast, our approach delivers real-time rendering capabilities while significantly reducing training time.

Gaussian Splatting. Recently, 3D Gaussian Splatting (3DGS) [15] has made significant strides toward real-time novel view synthesis. Unlike volume-based rendering, Gaussian Splatting uses efficient rasterization to render spatial Gaussian kernels, achieving real-time performance at 1080P resolution. Mip-Splatting [44] further introduces a 3D smoothing filter and a 2D Mip filter for alias-free renderings. Scaffold-GS [22] introduces structured 3D Gaussians to improve rendering efficiency and quality. [5] introduces triple splitting for efficient relighting. 2D Gaussian Splatting (2DGS) [11] replaces the 3D Gaussian kernels with 2D Gaussian that better align with 3D surfaces, leading to more accurate surface reconstruction. However, these methods face challenges in accurately modeling reflections due to their use of spherical harmonics (SH) to parameterize view-dependent effects based solely on viewing direction, which often results in blurry reflections. More recent works GaussianShader [12] and 3DGS-DR [16] try to incorporate additional environment maps to improve reflection modeling ability. However, these methods only consider distant lighting, ignoring near-field lighting, and are unable to capture high-frequency reflection details. 3iGS [32] extends 3D Gaussian Splatting by augmenting it with an illumination field using tensorial factorization, rendering final reflections through a neural renderer. However, this method is limited to bounded scenes, which restricts its applicability in real-world, unbounded environments. Our method adopts 2DGS as the scene representation and models environmental illumination using an additional set of environment Gaussian, which is rendered via our proposed Gaussian tracer. Our approach inherently supports high-frequency, near-field, and distant lighting in unbounded scenes, enabling detailed reflection rendering while maintaining real-time performance.

3. Preliminary

We begin by introducing 2D Gaussian Splatting (2DGS) [11], which our approach is built upon. 2DGS is an explicit scene representation similar to 3D Gaussian Splatting (3DGS) [15], which uses Gaussian primitives and rasterization to render screen projections. The key difference is that 2DGS represents the scene with a set of scaled 2D Gaussian primitives defined in a local tangent plane within world space by a transformation matrix \mathbf{H} :

$$\mathbf{H} = \begin{bmatrix} s_u \mathbf{t}_u & s_v \mathbf{t}_v & 0 & \mathbf{p}_k \\ 0 & 0 & 0 & 1 \end{bmatrix}, \quad (1)$$

where \mathbf{p}_k , $(\mathbf{t}_u, \mathbf{t}_v)$, and (s_u, s_v) denote the center, the two principal tangential vectors, and the scaling factors of the Gaussian, respectively.

To render an image, 2DGS employs the method described in [39] to determine the ray-primitive intersections.

These intersection points are subsequently utilized to compute the Gaussian’s contribution to the final image. The Gaussian properties are then integrated using a volume rendering algorithm to obtain the final pixel color:

$$\mathbf{c} = \sum_{i=1}^N T_i \alpha_i \mathbf{c}_i, \quad (2)$$

with

$$\alpha_i = \sigma_i \mathcal{G}_i \text{ and } T_i = \prod_{j=1}^{i-1} (1 - \alpha_j), \quad (3)$$

where $\mathcal{G}(\cdot)$ is the standard 2D Gaussian value evaluation.

Compared to 3D Gaussian, 2D Gaussian offers distinct advantages as a surface representation. First, the ray-splat intersection method adopted by 2DGS avoids multi-view depth inconsistency. Second, 2D Gaussian inherently provides a well-defined normal, which is essential for high-quality surface reconstruction and accurate reflection calculations. However, 2DGS relies on the limited representational capacity of Spherical Harmonics (SH) to model scene appearance, preventing it from capturing strong view-dependent effects like specular reflections, which leads to poor rendering results and “foggy” geometry [33]. To this end, we use the geometry-aligned 2D Gaussian primitives as the base scene representation and demonstrate how we effectively model complex reflections in the next section.

4. Method

Given a set of input images of a reflective scene, our goal is to reconstruct the 3D scene and synthesize photorealistic novel views in real-time. To achieve this, we propose utilizing *environment Gaussian* as an explicit 3D environment representation, which enables accurate modeling of complex reflections in real-world scenes. Additionally, we represent the scene geometry and base colors using another set of Gaussian primitives, denoted as *base Gaussian*. In this section, we first detail how *environment Gaussian* and *base Gaussian* work together to model complex reflections within the scene (Sec. 4.1). Then, We describe the design of a ray-tracing renderer that leverages the GPU’s RT cores to efficiently render and optimize the *environment Gaussian* (Sec. 4.2). Finally, we discuss our optimization process. (Sec. 4.3). An overview of our method is in Fig. 2.

4.1. Reflective Scenes Modeling

Gaussian splatting [11, 15] models appearance using Spherical Harmonics (SH), which has limited representation capacity for view-dependent effects. These limitations hinder its ability to capture complex, high-frequency specular reflections. Building on this observation, our key insight is that modeling reflections with a Gaussian environment representation can better model complex reflection ef-

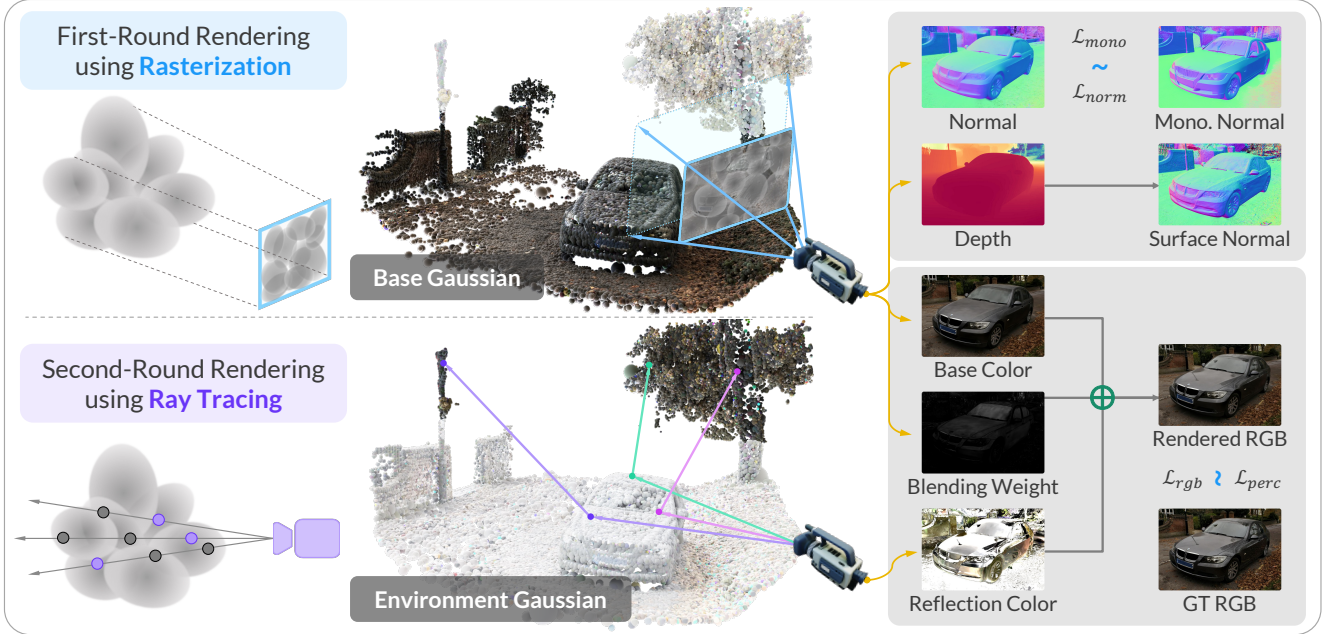


Figure 2. **Overview of EnvGS.** The rendering process begins by rasterizing the *base Gaussian* to obtain per-pixel normals, base colors, and blending weights. Next, we render the *environment Gaussian* in the reflection direction using our ray-tracing-based Gaussian renderer to capture the reflection colors. Finally, we combine the reflection and base colors for the final output. We jointly optimize the *environment Gaussian* and *base Gaussian* using monocular normals [42] and ground truth images for supervision.

facts while significantly reducing the complexity required for each Gaussian to capture intricate details within its SH.

Our proposed reflective scene representation includes two sets of 2D Gaussians: a *base Gaussian* \mathbf{P}_{base} for modeling the scene’s geometry and base appearance, and another *environment Gaussian* \mathbf{P}_{env} for capturing scene reflections. The basic parameterization of each Gaussian primitive is consistent with the original 2DGS [11], including 3D center position \mathbf{p} , opacity α , two principal tangential vectors $(\mathbf{t}_u, \mathbf{t}_v)$, a scaling vector (s_u, s_v) , and SH coefficients. To combine the two appearance components from the base and environment Gaussian into the final result, we introduce a blending weight for each base Gaussian.

The rendering process is performed in three steps. First, the base Gaussian \mathbf{P}_{base} is rendered using standard 2D Gaussian splatting to obtain the base color \mathbf{c}_{base} . By applying the volume rendering integration using Eq. (2), we also derive the surface position \mathbf{x} , surface normals \mathbf{n} , and blending weight β as:

$$v = \sum_{i \in \mathcal{N}} v_i \alpha_i \prod_{j=1}^{i-1} (1 - \alpha_j), v \in \{\mathbf{x}, \mathbf{n}, \beta\}. \quad (4)$$

Then, we compute the reflection direction \mathbf{d}_{ref} based on the camera ray direction \mathbf{d}_{cam} and the surface normal \mathbf{n} :

$$\mathbf{d}_{ref} = \mathbf{d}_{cam} - 2(\mathbf{d}_{cam} \cdot \mathbf{n})\mathbf{n}. \quad (5)$$

With the reflection direction \mathbf{d}_{ref} and surface point \mathbf{x} , the environment Gaussian \mathbf{P}_{env} is rendered using our differentiable Gaussian tracer to obtain the reflection color \mathbf{c}_{ref} , as detailed in Sec. 4.2. The final color is obtained through:

$$\mathbf{c} = (1 - \beta) \cdot \mathbf{c}_{base} + \beta \cdot \mathbf{c}_{ref}. \quad (6)$$

We blend the base color \mathbf{c}_{base} and reflection color \mathbf{c}_{ref} using the blending weight β . A visualization of \mathbf{c}_{base} and \mathbf{c}_{ref} can be found at Fig. 3.

Discussion. Compared to the environment map used by Gaussianshader [13] and 3DGS-DR [43], our explicit Gaussian environment representation offers several advantages. First, our method more accurately captures near-field reflections caused by occlusions from nearby objects. This improvement arises from explicitly modeling each Gaussian at its exact spatial location, thus avoiding the ambiguities and inaccuracies inherent in environment map representations that assume distant lighting. Second, by utilizing Gaussian primitives, EnvGS’s environment representation achieves greater expressiveness than low-frequency environment maps, enabling the capture of finer reflection details and enhancing rendering quality, as demonstrated by our experiments 5.3.

4.2. Differentiable Ray Tracing

Rendering the environment Gaussian with rasterization is impractical, as each pixel corresponds to a unique reflec-



Figure 3. **Visualization of reflection and base color.** Our method successfully reconstructs near-field and distant reflections using the *environment Gaussian* instead of baking into the base color.

tion ray and functions as a virtual camera. To address this, we draw on [25] and leverage the advanced optimizations of modern GPUs to design a novel, fully differentiable ray tracing framework. Built on OptiX [27], our framework achieves real-time rendering of 2,000,000 2DGS with a resolution of 1292x839 at 30 FPS on an RTX 4090 GPU.

In order to fully utilize the hardware acceleration for ray-primitive intersections, we need to convert each 2D Gaussian into a geometric primitive compatible with GPU processing and insert it into a bounding volume hierarchy (BVH). In light of this, we propose to represent each 2D Gaussian with two triangles. Specifically, we first define the four Gaussian bounding vertices $\mathbf{V}_{local} = \{\{\text{sgn}(r), \text{sgn}(r)\}\}$ in the local tangent plane, where $\text{sgn}(\cdot)$ is the sign function and r is set to 3 representing three times the sigma range. Then, the four local bounding vertices \mathbf{V}_{local} are transformed to world space as the vertices of the two triangles covering the Gaussian \mathbf{V}_{world} using Eq. 1. After the transformation, the triangles are organized into a BVH, which serves as the input for the ray tracing process.

We develop a custom CUDA kernel using the *raygen* and *anyhit* programmable entry points of OptiX. Inspired by [25], the rendering is done in a chunk-by-chunk manner. The *anyhit* kernel traces the input ray to obtain a chunk of size k , while *raygen* integrates this chunk and invokes *anyhit* to retrieve the next chunk along the ray. Specifically, consider an input ray with origin \mathbf{o} and direction \mathbf{d} . The *raygen* program first initiates a traversal against the BVH to identify all possible intersections along the ray. During the traversal, the *anyhit* program sorts each intersected Gaussian by the depth and maintains a sorted k -buffer for the closest k intersections. We empirically found that k with 16 is the best trade-off between traversal counts and the number of Gaussians sorted per traversal. After traversal, the

raygen program integrates properties of the sorted Gaussians in the buffer following Eq. 2. The Gaussian response is calculated by applying the inverse of the transformation matrix \mathbf{H} to the ray’s intersection point \mathbf{x}_i and evaluating the Gaussian value at the transformed point as:

$$\mathcal{G}_i(\mathbf{u}_i) = \mathcal{G}_i(\mathbf{H}^{-1}\mathbf{x}_i). \quad (7)$$

This process repeats until no further intersections are found along the ray or the accumulated transmittance drops below a specified threshold. More details can be found in supplementary materials.

Our ray tracing framework is fully differentiable, allowing for end-to-end optimization of both the base and the environment Gaussian primitives. However, storing all intersections during the forward pass and performing the backward pass in back-to-front order, as done in 3DGS [15], is impractical due to high memory consumption. To address this, we implement the backward pass in the same front-to-back order as the forward pass by re-casting rays and computing gradients for each integration step. A key aspect is calculating the gradient with respect to the input ray origin $\frac{\partial \mathcal{L}}{\partial \mathbf{o}}$ and direction $\frac{\partial \mathcal{L}}{\partial \mathbf{d}}$, which is crucial for the joint optimization of our model (see supplementary for more details). Our ablation in Sec 5.4 demonstrates that this joint optimization of geometry and appearance is essential for recovering geometrically accurate surfaces.

4.3. Optimization

To enhance training stability, we initiate optimization by first training the base Gaussian \mathbf{P}_{base} , which is initialized using the sparse point cloud obtained from Structure-from-Motion (SfM) [10, 30]. After the bootstrapping phase, we initialize the environment Gaussian \mathbf{P}_{env} by partitioning the scene’s bounding box \mathbf{B}_{scene} into N^3 sub-grids and randomly sampling K primitives within each grid, and then optimize the base Gaussian and environment Gaussian jointly. The scene’s bounding box \mathbf{B}_{scene} is determined by the 99.5% quantile of the sparse point cloud’s bounding box \mathbf{B}_{sfm} obtained from SfM, the sub-grids resolution N is set to 32, and K is set to 5 for each grid.

We follow 2DGS [11] to add a normal consistency constraint between the rendered normal map \mathbf{n} and the gradients of the depth map \mathbf{N}_d :

$$\mathcal{L}_{norm} = \frac{1}{N_p} \sum_{i=1}^{N_p} (1 - \mathbf{n}_i^\top \mathbf{N}_d), \quad (8)$$

where N_p is the number of pixels in the image and \mathbf{N}_d is calculated as finite differences of neighboring pixels in the depth map:

$$\mathbf{N}_d(\mathbf{u}) = \frac{\nabla_u \mathbf{P}_d \times \nabla_v \mathbf{P}_d}{\|\nabla_u \mathbf{P}_d \times \nabla_v \mathbf{P}_d\|}. \quad (9)$$

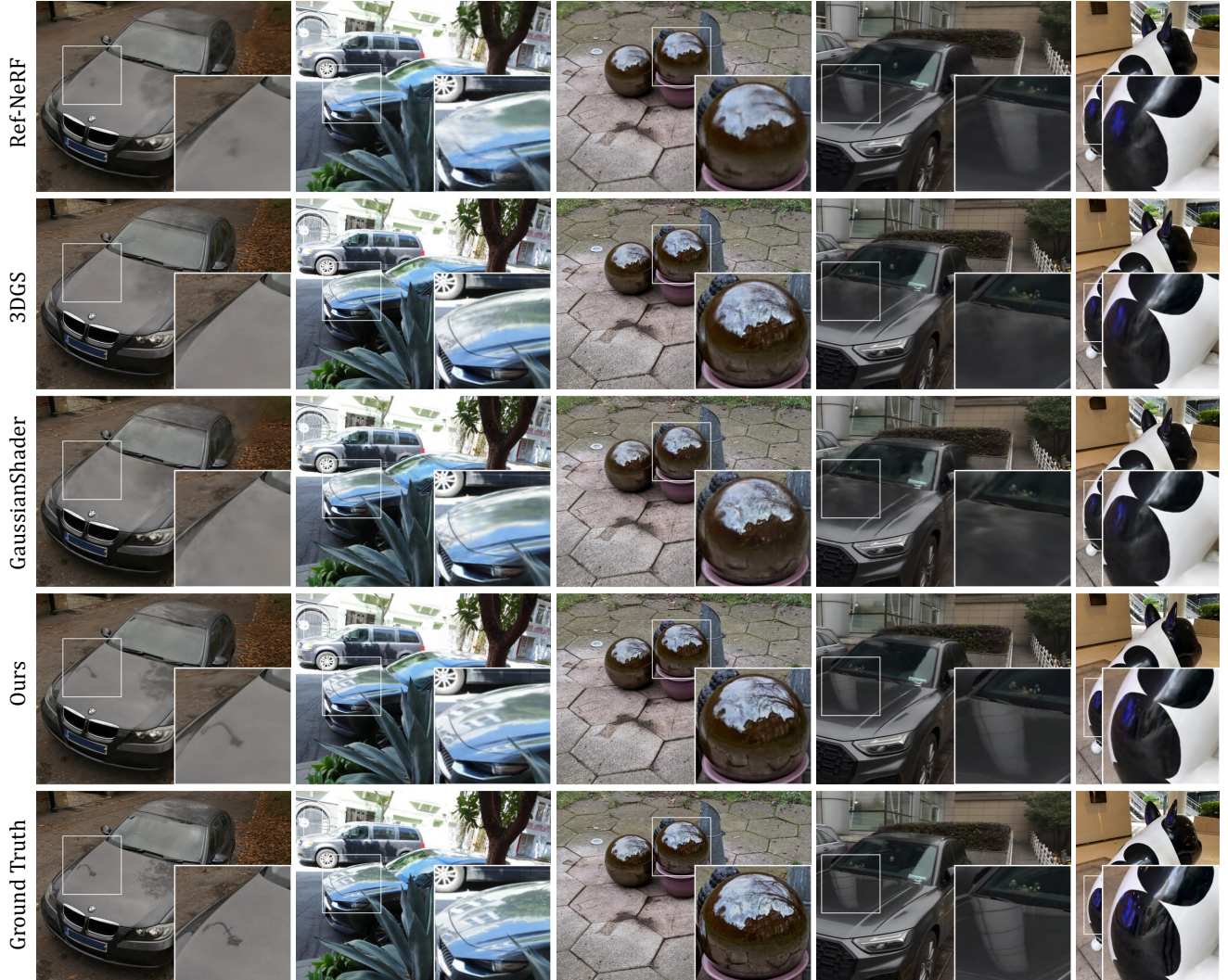


Figure 4. **Qualitative comparison on real scenes.** Our method significantly improves rendering quality over previous approaches, particularly in producing more detailed reflections. Zoom in for more details.

However, the normal consistency constraint alone is insufficient for accurately modeling ambiguous surfaces involving both reflection and refraction. Inspired by recent advances in monocular normal estimation [1, 9, 42], we propose to supervise the rendered normal map \mathbf{n} using monocular normal estimates \mathbf{N}_m :

$$\mathcal{L}_{mono} = \frac{1}{N_p} \sum_{i=1}^{N_p} (1 - \mathbf{n}_i^\top \mathbf{N}_m). \quad (10)$$

In addition to the \mathcal{L}_1 image loss and D-SSIM loss \mathcal{L}_{ssim} employed by 3DGS [15], we also use perceptual loss [45] to enhance the perceived quality of the rendered image:

$$\mathcal{L}_{perc} = \|\Phi(\mathbf{I}) - \Phi(\mathbf{I}_{gt})\|_1, \quad (11)$$

where Φ is the pre-trained VGG-16 network [29] and $\mathbf{I}, \mathbf{I}_{gt}$

are the rendered and ground truth images, respectively.

The final loss function is defined as:

$$\mathcal{L} = \mathcal{L}_{rgb} + \lambda_1 \mathcal{L}_{norm} + \lambda_2 \mathcal{L}_{mono} + \lambda_3 \mathcal{L}_{perc}, \quad (12)$$

where \mathcal{L}_{rgb} is the photometric reconstruction loss combining the \mathcal{L}_1 loss and a D-SSIM [38] term with a ratio of 0.8 and 0.2 respectively. We set $\lambda_1 = 0.04$, $\lambda_2 = 0.01$, and $\lambda_3 = 0.01$ across our experiments.

5. Experiments

5.1. Implementation Details

We implement EnvGS with custom OptiX kernels and optimize our model using the PyTorch framework [28, 40] with the Adam optimizer [17]. Specifically, we set the learning

	Methods	Ref-NeRF Real Scenes			NeRF-Casting Shiny Scenes			FPS \uparrow
		PSNR \uparrow	SSIM \uparrow	LPIPS \downarrow	PSNR \uparrow	SSIM \uparrow	LPIPS \downarrow	
Non Real-time	Ref-NeRF* [33]	23.087	0.625	0.261	30.583	0.890	0.124	<0.1
	UniSDF [35]	23.700	0.635	0.266	30.838	0.889	0.130	<0.1
	ZipNeRF [4]	23.677	0.635	0.247	31.740	0.904	0.105	<0.1
	NeRF-Casting [34]	24.670	0.659	0.246	31.023	0.889	0.128	<0.1
Real-time	3DGS [15]	23.700	0.641	0.262	28.860	0.877	0.159	182.307
	2DGS [11]	23.804	0.654	0.281	28.276	0.862	0.193	159.188
	GaussianShader [12]	22.875	0.622	0.314	26.412	0.835	0.216	27.945
	3DGS-DR [43]	23.522	0.640	0.274	28.487	0.858	0.197	133.593
	Ours	24.617	0.671	0.241	30.444	0.886	0.148	26.221

Table 1. **Quantitative comparison on Ref-Real [33] and NeRF-Casting Shiny Scenes [34] datasets.** Our method delivers the highest rendering quality among real-time techniques and outperforms several non-real-time methods, achieving competitive results with the state-of-the-art non-real-time method NeRF-Casting [34], while being 100 times faster. Note that Ref-NeRF* is an improved version of Ref-NeRF [33] that uses Zip-NeRF’s geometry model. All metrics are evaluated at 1/4 resolution as prior works [34].

rates for the parameters of each base and environment Gaussian to match those used in 2DGS [11]. The learning rate for the blending weight is set to $1e^{-2}$. During training, we apply the adaptive Gaussian control strategy of 3DGS [15] with the normal propagation and color sabotage introduced in 3DGS-DR [16]. Since our Gaussian tracer integrates the Gaussian properties directly in 3D space, there is no valid gradient for the projected 2D center, which is used as the densification criterion in 3DGS. Following [25], we accumulate the 3D spatial gradients of the Gaussian position to achieve a similar effect. Note that each accumulated gradient is scaled by half of the intersection depth to prevent under-densification in distant regions. All experiments are conducted on a single NVIDIA RTX 4090 GPU.

5.2. Datasets and Evaluation Metrics

We train and evaluate EnvGS on a range of datasets with a focus on real-world scenes characterized by complex view-dependent effects. We evaluate the Ref-Real [33] and NeRF-Casting Shiny Scenes [34] to demonstrate our method’s ability for complex specular reflections in real-world scenes. We additionally captured two more real-world scenes for a more comprehensive evaluation. We demonstrate that our methods can reconstruct detailed reflections on complex real-world scenes with real-time rendering speed. Additionally, we evaluate our method on the synthetic Shiny Blender dataset [33], which is rendered using environment maps. More evaluation results can be found in the supplementary materials.

We maintain consistent training and testing splits and image resolution across all datasets, following prior works [3, 15, 33]. We use three commonly used metrics for evaluation: PSNR, SSIM [38], and LPIPS [45].

5.3. Baseline Comparisons

We compare our method with both implicit and explicit prior works, including Zip-NeRF [11], 3DGS [15], 2DGS [11], which are designed for general scenes with primarily diffuse appearances, as well as with methods specif-

	Audi			Dog		
	PSNR \uparrow	SSIM \uparrow	LPIPS \downarrow	PSNR \uparrow	SSIM \uparrow	LPIPS \downarrow
Ref-NeRF [33]	27.078	0.761	0.341	23.620	0.673	0.389
3DGS [15]	26.406	0.835	0.168	25.300	0.882	0.165
2DGS [11]	26.057	0.831	0.190	24.933	0.876	0.184
GaussianShader [12]	25.113	0.809	0.216	23.061	0.840	0.226
3DGS-DR [43]	26.368	0.831	0.191	23.943	0.850	0.210
Ours	27.604	0.847	0.151	25.599	0.885	0.151

Table 2. **Quantitative results on our self-captured scenes.**

ically tailored for scenes with strong specular reflections, including Ref-NeRF [33], GaussianShader [12] and 3DGS-DR [16]. We also compare our approach with the more recent implicit method NeRF-Casting [34].

In this section, we present quantitative and qualitative results to illustrate the advantages of our methods. Since accurate reflection reconstruction and rendering are the essential advantages of our method, we encourage readers to refer to the various rendered continuous video results in the supplementary material for a more comprehensive evaluation of our method.

We first evaluate our method on nine real-world scenes from the Ref-Real dataset [33], NeRF-Casting Shiny Scenes [34] and our self-captured real-world scenes, which feature complex geometry and specular reflections. The quantitative results, shown in Tab. 1 and Tab. 2, demonstrate that our method outperforms all explicit methods by a large margin and achieves comparable results to the current state-of-the-art implicit method, NeRF-Casting, while being significantly faster. The qualitative results in Fig.4 further highlight the superior performance of our method in capturing complex view-dependent effects, especially near-field reflections and high-frequency details.

We provide additional comparisons on the Mip-NeRF 360 dataset [3] and the Shiny Blender dataset [33] in the supplementary material, which also includes per-scene metric breakdowns from Tab. 1. Our method achieves competitive results on both datasets, demonstrating its versatility and effectiveness in handling diverse real-world scenes with complex view-dependent effects.

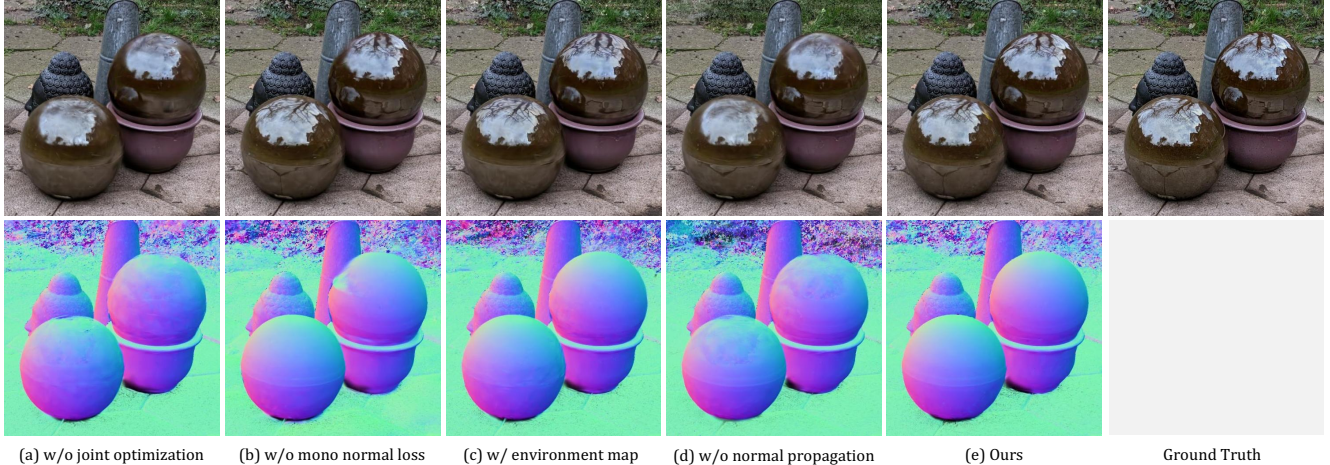


Figure 5. **Ablation study of proposed components on the Ref-Real dataset [33].** Removing either the monocular normal constraint or the joint optimization of base and environment Gaussians results in noisy geometry and inaccurate reflection reconstruction. The “w/ environment map” variant fails to capture near-field reflections.

5.4. Ablation Studies

	PSNR \uparrow	SSIM \uparrow	LPIPS \downarrow
w/o joint optimization	24.034	0.644	0.287
w/o mono normal loss	24.107	0.648	0.270
w/ environment map	24.145	0.646	0.285
w/o color sabotage	24.268	0.650	0.269
w/o normal propagation	24.192	0.652	0.271
Ours	24.546	0.662	0.251

Table 3. **Ablation studies.**

In this section, we conduct ablation studies of our key components on the Ref-Real dataset. Quantitative and qualitative results are shown in Tab. 3 and Fig. 5, respectively.

Joint optimization. The “w/o joint optimization” variant detaches the joint optimization of the *base Gaussian* and *environment Gaussian* from the reflection rendering step. As shown in Tab. 3 and Fig. 5, This variant fails to recover accurate geometry, leading to inferior reflection reconstruction and rendering quality.

Monocular normal constraint The “w/o monocular normal” variant removes the monocular normal constraint as described in Sec. 4.3. Training may become trapped in largely incorrect geometry, resulting in inaccurate reflection reconstruction, as demonstrated in Tab.3 and Fig.5.

Environment map representation The “w/ environment map” variant replaces our core Gaussian environment representation with an environment map representation while keeping all other components unchanged. Figure 5 illustrates that while it effectively captures smooth distant reflections, it has difficulty modeling near-field and high-frequency reflections, and produces more bumpy geometry.

Color sabotage and normal propagation. The “w/o color sabotage” and “w/o normal propagation” variants omit

the color sabotage and normal propagation steps from our method, respectively. As demonstrated in Tab. 3, both variants result in reduced rendering quality.

The Necessity of using a separate environment Gaussian primitives. To evaluate the decision to use separate Gaussian primitives for reflection modeling, we perform an experiment using a single set of Gaussian primitives for both reflection and base scene modeling. We first trace a camera ray to obtain the base color, normal and rendering weight, then trace a secondary ray to render the reflection color, ultimately combining these results using Eq. (6) to get the final color. However, we found that the experiment consistently failed to converge due to unavoidable interference between suboptimal geometry during optimization and incorrectly hitting Gaussian primitives from erroneous reflection directions, leading to an unstable training process.

6. Conclusion and Discussion

This paper introduced EnvGS, a novel reflective scene representation for high-quality complex reflection capturing and real-time rendering. Our method explicitly models reflections with a set of *environment Gaussian* primitives. The environment Gaussian primitives are used together with a set of base Gaussian primitives that model basic scene properties (geometry, base color, and blending weight) to model the appearance of the whole scene. Furthermore, we develop a differentiable Gaussian ray tracer utilizing GPU’s RT core to effectively optimize and render the *environment Gaussian*. The proposed method demonstrates superior performance in capturing complex reflections across various datasets.

A limitation of EnvGS is its difficulty with transparent and refractive materials, as it only addresses reflection di-

rection. Future work could explore extending our method to accommodate these materials.

References

- [1] Gwangbin Bae and Andrew J. Davison. Rethinking inductive biases for surface normal estimation. In *IEEE/CVF Conference on Computer Vision and Pattern Recognition (CVPR)*, 2024. 6
- [2] Jonathan T. Barron, Ben Mildenhall, Matthew Tancik, Peter Hedman, Ricardo Martin-Brualla, and Pratul P. Srinivasan. Mip-nerf: A multiscale representation for anti-aliasing neural radiance fields, 2021. 2
- [3] Jonathan T. Barron, Ben Mildenhall, Dor Verbin, Pratul P. Srinivasan, and Peter Hedman. Mip-nerf 360: Unbounded anti-aliased neural radiance fields. *CVPR*, 2022. 7, 1
- [4] Jonathan T. Barron, Ben Mildenhall, Dor Verbin, Pratul P. Srinivasan, and Peter Hedman. Zip-nerf: Anti-aliased grid-based neural radiance fields. *ICCV*, 2023. 2, 7, 1, 5
- [5] Zoubin Bi, Yixin Zeng, Chong Zeng, Fan Pei, Xiang Feng, Kun Zhou, and Hongzhi Wu. Gs3: Efficient relighting with triple gaussian splatting. In *SIGGRAPH Asia 2024 Conference Papers*, pages 1–12, 2024. 3
- [6] Anpei Chen, Zexiang Xu, Andreas Geiger, Jingyi Yu, and Hao Su. Tensorf: Tensorial radiance fields. In *European Conference on Computer Vision (ECCV)*, 2022. 2
- [7] Sara Fridovich-Keil, Alex Yu, Matthew Tancik, Qinhong Chen, Benjamin Recht, and Angjoo Kanazawa. Plenoxels: Radiance fields without neural networks. In *CVPR*, 2022. 2
- [8] Chen Guangcheng, He Yicheng, He Li, and Zhang Hong. Pidr: Polarimetric neural implicit surface reconstruction for textureless and specular objects. In *Proceedings of the European Conference on Computer Vision (ECCV)*, 2024. 2
- [9] Jing He, Haodong Li, Wei Yin, Yixun Liang, Leheng Li, Kaiqiang Zhou, Hongbo Liu, Bingbing Liu, and Yingcong Chen. Lotus: Diffusion-based visual foundation model for high-quality dense prediction. *arXiv preprint arXiv:2409.18124*, 2024. 6
- [10] Xingyi He, Jiaming Sun, Yifan Wang, Sida Peng, Qixing Huang, Hujun Bao, and Xiaowei Zhou. Detector-free structure from motion. In *Proceedings of the IEEE/CVF Conference on Computer Vision and Pattern Recognition*, pages 21594–21603, 2024. 5
- [11] Binbin Huang, Zehao Yu, Anpei Chen, Andreas Geiger, and Shenghua Gao. 2d gaussian splatting for geometrically accurate radiance fields. In *ACM SIGGRAPH 2024 Conference Papers*, pages 1–11, 2024. 3, 4, 5, 7, 6
- [12] Yingwenqi Jiang, Jiadong Tu, Yuan Liu, Xifeng Gao, Xiaoxiao Long, Wenping Wang, and Yuexin Ma. Gaussianshader: 3d gaussian splatting with shading functions for reflective surfaces. *arXiv preprint arXiv:2311.17977*, 2023. 3, 7, 5, 6
- [13] Yingwenqi Jiang, Jiadong Tu, Yuan Liu, Xifeng Gao, Xiaoxiao Long, Wenping Wang, and Yuexin Ma. Gaussian-shader: 3d gaussian splatting with shading functions for reflective surfaces. In *Proceedings of the IEEE/CVF Conference on Computer Vision and Pattern Recognition*, pages 5322–5332, 2024. 2, 4, 1
- [14] James T Kajiya and Brian P Von Herzen. Ray tracing volume densities. *ACM SIGGRAPH computer graphics*, 18(3):165–174, 1984. 2
- [15] Bernhard Kerbl, Georgios Kopanas, Thomas Leimkühler, and George Drettakis. 3d gaussian splatting for real-time radiance field rendering. *ACM Transactions on Graphics*, 42(4), 2023. 1, 3, 5, 6, 7, 2
- [16] Ye Keyang, Hou Qiming, and Zhou Kun. 3d gaussian splatting with deferred reflection. 2024. 3, 7, 1
- [17] Diederik P Kingma. Adam: A method for stochastic optimization. *arXiv preprint arXiv:1412.6980*, 2014. 6
- [18] Zhaoshuo Li, Thomas Müller, Alex Evans, Russell H Taylor, Mathias Unberath, Ming-Yu Liu, and Chen-Hsuan Lin. Neuralangelo: High-fidelity neural surface reconstruction. In *IEEE Conference on Computer Vision and Pattern Recognition (CVPR)*, 2023. 2
- [19] Ruofan Liang, Huiting Chen, Chunlin Li, Fan Chen, Selvakumar Panneer, and Nandita Vijaykumar. Envidr: Implicit differentiable renderer with neural environment lighting. *arXiv preprint arXiv:2303.13022*, 2023. 2
- [20] Lingjie Liu, Jiatao Gu, Kyaw Zaw Lin, Tat-Seng Chua, and Christian Theobalt. Neural sparse voxel fields. *NeurIPS*, 2020. 2
- [21] Yuan Liu, Peng Wang, Cheng Lin, Xiaoxiao Long, Jiepeng Wang, Lingjie Liu, Taku Komura, and Wenping Wang. Nero: Neural geometry and brdf reconstruction of reflective objects from multiview images. In *SIGGRAPH*, 2023. 2
- [22] Tao Lu, Mulin Yu, Linning Xu, Yuanbo Xiangli, Limin Wang, Dahua Lin, and Bo Dai. Scaffold-gs: Structured 3d gaussians for view-adaptive rendering. In *Proceedings of the IEEE/CVF Conference on Computer Vision and Pattern Recognition*, pages 20654–20664, 2024. 3
- [23] Li Ma, Vasu Agrawal, Haithem Turki, Changil Kim, Chen Gao, Pedro Sander, Michael Zollhöfer, and Christian Richardt. Specnerf: Gaussian directional encoding for specular reflections, 2023. 2
- [24] Ben Mildenhall, Pratul P. Srinivasan, Matthew Tancik, Jonathan T. Barron, Ravi Ramamoorthi, and Ren Ng. Nerf: Representing scenes as neural radiance fields for view synthesis. In *ECCV*, 2020. 1, 2
- [25] Nicolas Moenne-Loccoz, Ashkan Mirzaei, Or Perel, Ricardo de Lutio, Janick Martinez Esturo, Gavriel State, Sanja Fidler, Nicholas Sharp, and Zan Gojcic. 3D Gaussian Ray Tracing: Fast tracing of particle scenes. *ACM Transactions on Graphics and SIGGRAPH Asia*, 2024. 5, 7
- [26] Thomas Müller, Alex Evans, Christoph Schied, and Alexander Keller. Instant neural graphics primitives with a multiresolution hash encoding. *ACM Trans. Graph.*, 41(4):102:1–102:15, 2022. 2
- [27] Steven G Parker, James Bigler, Andreas Dietrich, Heiko Friedrich, Jared Hoberock, David Luebke, David McAllister, Morgan McGuire, Keith Morley, Austin Robison, et al. Optix: a general purpose ray tracing engine. *Acm transactions on graphics (tog)*, 29(4):1–13, 2010. 2, 5
- [28] Adam Paszke, Sam Gross, Francisco Massa, Adam Lerer, James Bradbury, Gregory Chanan, Trevor Killeen, Zeming

- Lin, Natalia Gimelshein, Luca Antiga, et al. Pytorch: An imperative style, high-performance deep learning library. *Advances in neural information processing systems*, 32, 2019. 6
- [29] Karen Simonyan and Andrew Zisserman. Very deep convolutional networks for large-scale image recognition. *arXiv preprint arXiv:1409.1556*, 2014. 6
- [30] Noah Snavely, Steven M Seitz, and Richard Szeliski. Photo tourism: exploring photo collections in 3d. In *ACM siggraph 2006 papers*, pages 835–846. 2006. 5
- [31] Cheng Sun, Min Sun, and Hwann-Tzong Chen. Direct voxel grid optimization: Super-fast convergence for radiance fields reconstruction. In *CVPR*, 2022. 2
- [32] Zhe Jun Tang and Tat-Jen Cham. 3igs: Factorised tensorial illumination for 3d gaussian splatting. *arXiv preprint arXiv:2408.03753*, 2024. 3, 6
- [33] Dor Verbin, Peter Hedman, Ben Mildenhall, Todd Zickler, Jonathan T. Barron, and Pratul P. Srinivasan. Ref-NeRF: Structured view-dependent appearance for neural radiance fields. *CVPR*, 2022. 2, 3, 7, 8, 1, 5, 6
- [34] Dor Verbin, Pratul P Srinivasan, Peter Hedman, Ben Mildenhall, Benjamin Attal, Richard Szeliski, and Jonathan T Barron. Nerf-casting: Improved view-dependent appearance with consistent reflections. *arXiv preprint arXiv:2405.14871*, 2024. 2, 7, 1, 3, 5, 6
- [35] Fangjinhua Wang, Marie-Julie Rakotosaona, Michael Niemeyer, Richard Szeliski, Marc Pollefeys, and Federico Tombari. Unisdf: Unifying neural representations for high-fidelity 3d reconstruction of complex scenes with reflections. In *NeurIPS*, 2024. 2, 7, 5, 6
- [36] Peng Wang, Lingjie Liu, Yuan Liu, Christian Theobalt, Taku Komura, and Wenping Wang. Neus: Learning neural implicit surfaces by volume rendering for multi-view reconstruction. *NeurIPS*, 2021. 2
- [37] Yiming Wang, Qin Han, Marc Habermann, Kostas Daniilidis, Christian Theobalt, and Lingjie Liu. Neus2: Fast learning of neural implicit surfaces for multi-view reconstruction. In *Proceedings of the IEEE/CVF International Conference on Computer Vision (ICCV)*, 2023. 2
- [38] Zhou Wang, Alan C Bovik, Hamid R Sheikh, and Eero P Simoncelli. Image quality assessment: from error visibility to structural similarity. *IEEE transactions on image processing*, 13(4):600–612, 2004. 6, 7
- [39] Tim Weyrich, Simon Heinzle, Timo Aila, Daniel B Fasnacht, Stephan Oetiker, Mario Botsch, Cyril Flaig, Simon Mall, Kaspar Rohrer, Norbert Felber, et al. A hardware architecture for surface splatting. *ACM Transactions on Graphics (TOG)*, 26(3):90–es, 2007. 3
- [40] Zhen Xu, Tao Xie, Sida Peng, Haotong Lin, Qing Shuai, Zhiyuan Yu, Guangzhao He, Jiaming Sun, Hujun Bao, and Xiaowei Zhou. Easyvolcap: Accelerating neural volumetric video research. In *SIGGRAPH Asia 2023 Technical Communications*, pages 1–4. 2023. 6
- [41] Lior Yariv, Yoni Kasten, Dror Moran, Meirav Galun, Matan Atzmon, Basri Ronen, and Yaron Lipman. Multiview neural surface reconstruction by disentangling geometry and appearance. *Advances in Neural Information Processing Systems*, 33, 2020. 2
- [42] Chongjie Ye, Lingteng Qiu, Xiaodong Gu, Qi Zuo, Yushuang Wu, Zilong Dong, Liefeng Bo, Yuliang Xiu, and Xiaoguang Han. Stablenormal: Reducing diffusion variance for stable and sharp normal. *ACM Transactions on Graphics*, 2024. 4, 6
- [43] Keyang Ye, Qiming Hou, and Kun Zhou. 3d gaussian splatting with deferred reflection. In *ACM SIGGRAPH 2024 Conference Papers*, pages 1–10, 2024. 2, 4, 7, 1, 5, 6
- [44] Zehao Yu, Anpei Chen, Binbin Huang, Torsten Sattler, and Andreas Geiger. Mip-splatting: Alias-free 3d gaussian splatting. *Conference on Computer Vision and Pattern Recognition (CVPR)*, 2024. 3
- [45] Richard Zhang, Phillip Isola, Alexei A Efros, Eli Shechtman, and Oliver Wang. The unreasonable effectiveness of deep features as a perceptual metric. In *Proceedings of the IEEE conference on computer vision and pattern recognition*, pages 586–595, 2018. 6, 7

EnvGS: Modeling View-Dependent Appearance with Environment Gaussian

Supplementary Material

In the supplementary material, we provide more qualitative and quantitative results and per-scene breakdowns to demonstrate the effectiveness and robustness of our method (Sec. A). We also provide additional ablation studies to further analyze the key components of our method (Sec. B). Furthermore, we provide details on the gradient computation of our Gaussian tracer (Sec. C).

Accurate and smooth reflection reconstruction and rendering are key advantages of our method. We strongly encourage readers to view the rendered continuous videos in the supplementary material for a more comprehensive understanding of its performance.

A. Additional Results

A.1. Comparisons on Real-World Reflective Scenes

We present additional qualitative comparisons on the NeRF-Casting Shiny Scenes [34], which include both indoor and outdoor real-world scenes featuring complex reflections. As shown in Fig. 7, our method significantly outperforms previous approaches in reflection fidelity and overall rendering quality, particularly excelling in near-field reflections and high-frequency reflection details.

We also provide per-scene breakdowns of Ref-Real [33] and NeRF-Casting Shiny Scenes [34] in Tab. 5. These results are consistent with the averaged results in the paper. All metrics are evaluated at the original resolution downsampled by a factor of 4, following prior works [34]. Notably, our method is more general and does not rely on manually estimated bounding boxes for foreground objects, which are essential for 3DGS-DR [43] to prevent optimization failure.

A.2. Comparisons on Shiny Blender [33]

In Tab. 6, Fig. 8 and Fig. 9, we present additional quantitative and qualitative comparisons on the Shiny Blender dataset [34], which is rendered with environment maps under distant lighting assumption. The results show that although being designed for robustness on real-world data, our method effectively reconstructs accurate distant specular reflections, performing on par with or surpassing prior methods GaussianShader [13] and 3DGS-DR [16] specifically designed for environment map lighting scenarios. EnvGS considerably outperforms these methods in capturing near-field reflections caused by self-occlusions, as illustrated in the zoomed-in regions of the “toaster” scene. Moreover, our method reconstructs more accurate geometry, as shown in Fig. 9.

A.3. Comparisons on Mip-NeRF 360 [3]

We perform additional comparisons on the Mip-NeRF 360 dataset [3], which consists of large-scale real-world scenes with primarily diffuse appearance and complex geometry. As shown in Tab. 7, our method is not limited to reflective scenes and can achieve comparable or superior performance to both state-of-the-art implicit [4] and explicit [15] methods.

B. Additional Ablation Studies

B.1. Environment Representation Comparison



Figure 6. **Qualitative comparison between the environment map representation and our environment Gaussian representation.** Replacing the environment map with our environment Gaussian representation significantly improves the rendering quality, especially in capturing near-field reflections and high-frequency reflection details.

As described in Sec. 5.4, the environment representation plays a crucial role in capturing complex reflections. In Fig. 6, we provide additional qualitative comparisons between our *environment Gaussian* representation and the environment map representation. The “w/ env. map 128” and “w/ env. map 256” variants replace our core *environment Gaussian* representation with environment maps using six cubemaps at resolutions of 128 and 256, respectively. The results demonstrate that both environment map variants fail to capture the near-field reflections and tend to blur

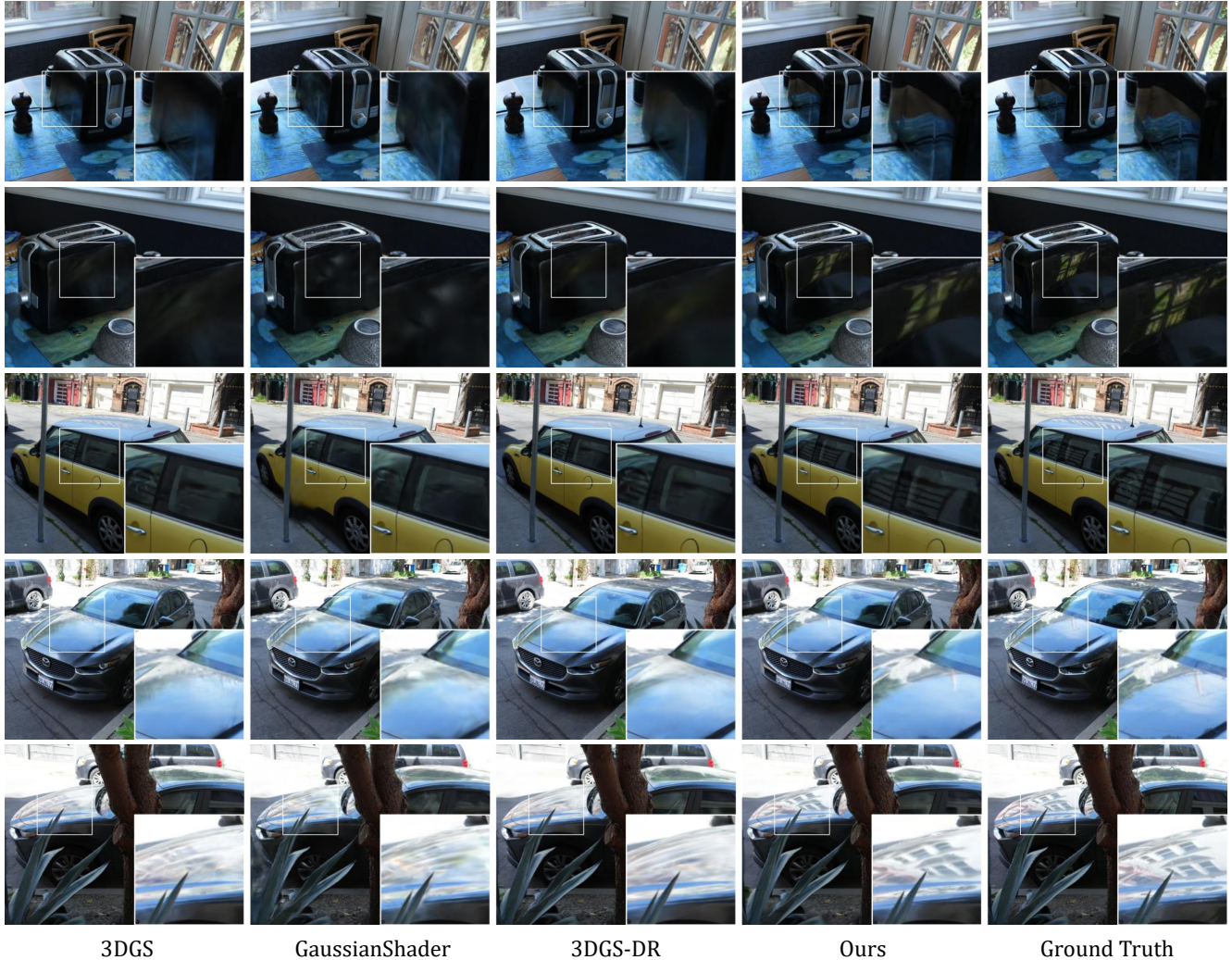


Figure 7. **Qualitative comparison on real scenes.** Our method significantly improves rendering quality over previous approaches, particularly in producing more detailed reflections. Zoom in for more details.

high-frequency reflection details, whereas our *environment Gaussian* representation excels at capturing complex reflections with high fidelity.

B.2. Speed Analysis

We conduct additional speed ablations on the “*hatchback*” from the NeRF-Casting Shiny Scenes [34] with resolution 3504×2336 (which we downsample by a factor of 4, as done in all baselines and experiments). The results are listed in Tab. 4.

Differentiable Gaussian tracing. As discussed in Sec. 4.2, rendering the *environment Gaussian* primitives with rasterization is impractical due to the uniqueness of each reflected ray. To validate this, we compare two alternative rendering strategies: (1) manually computing the ray-primitive intersections using PyTorch in a chunk-based manner (“w/ Py-

Torch”), and (2) rasterizing the *environment Gaussian* primitives with a modified 3DGS [15] rasterizer using 1×1 tiles (“w/ 1×1 -tile rasterizer”). All three methods, including our Gaussian tracer, apply the same volume rendering equation as in Eq. 2. Quantitative results in Tab. 4 reveal that both alternative strategies take over an hour to render a single frame, whereas our Gaussian tracer achieves real-time rendering speeds, leveraging hardware-accelerated ray tracing.

Rendering speed analysis. As mentioned in Sec. 4.1, the rendering of our method consists of two main rounds: rasterization of the *base Gaussian* and ray tracing of the *environment Gaussian*, the final color is the blending of the two. Based on the fact that only a small portion of the scene surface contains strong specular reflections, we can further accelerate the rendering process by only tracing rays with high blending weights, which are only made possible

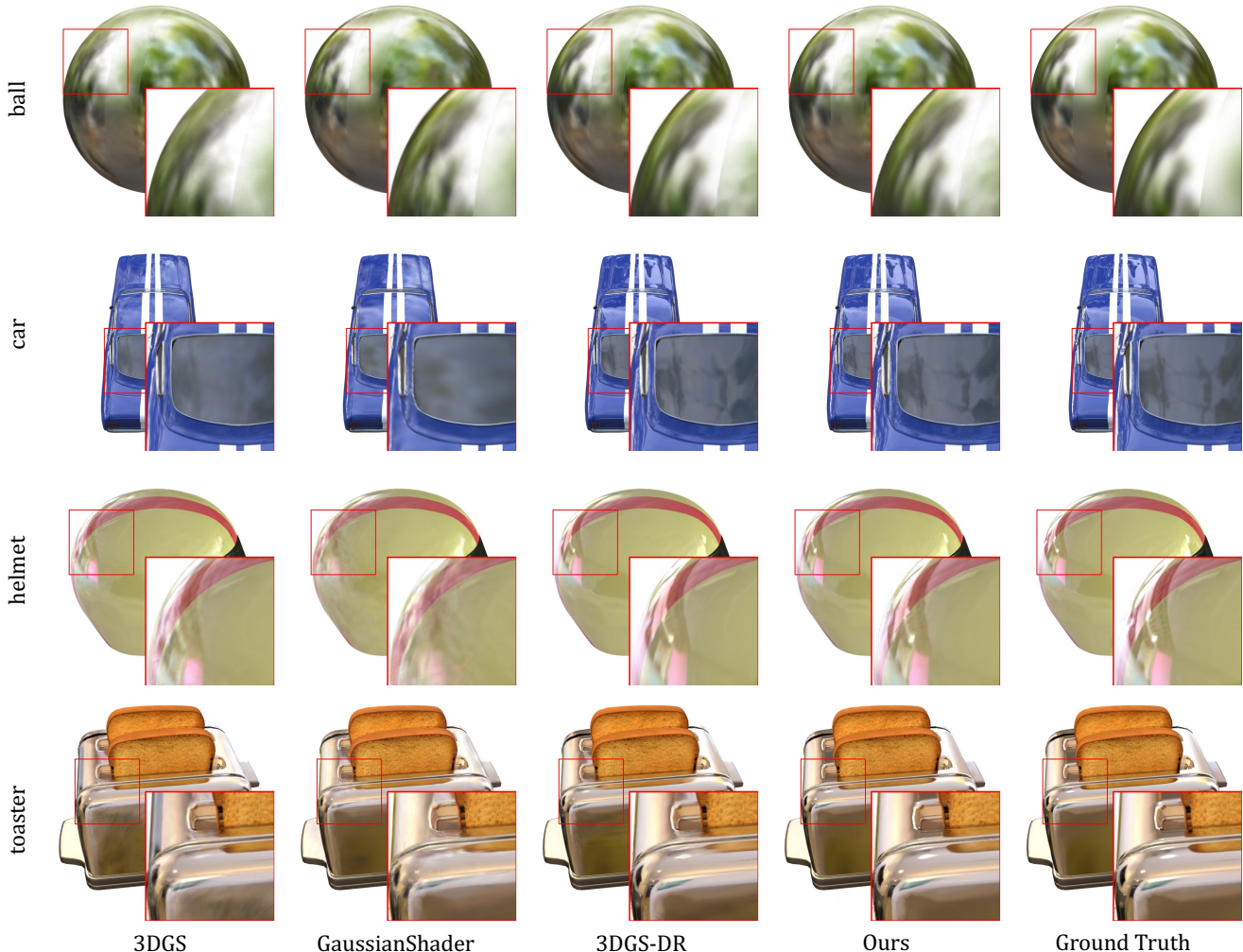


Figure 8. **Qualitative comparison on synthetic scenes.** Despite being designed for robustness on real-world data, our method effectively reconstructs accurate distant specular reflections and effectively captures near-field reflections caused by self-occlusions.

	PSNR \uparrow	SSIM \uparrow	LPIPS \downarrow	FPS \uparrow
w/ PyTorch	-	-	-	1/6157.613
w/ 1x1-tile rasterizer	-	-	-	1/11902.431
w/ 50% weight filting	27.137	0.824	0.192	36.216
w/ 75% weight filting	27.104	0.823	0.192	41.824
w/ 80% weight filting	27.033	0.822	0.193	44.215
w/ 90% weight filting	26.695	0.816	0.197	47.149
Ours	27.139	0.824	0.191	32.259

Table 4. **Runtime analysis of the proposed method on the *hatchback* of NeRF-Casting Shiny Scenes [34].** Rasterization or PyTorch-based ray tracing is impractical for rendering the *environment Gaussian* primitives. The acceleration techniques lead to minimal quality changes as shown by the cell.

by our tracing-based renderer. We ablate the effectiveness and quality impact of this acceleration technique, results are shown in Tab. 4.

C. Details of Gradient Computation

To enable the joint optimization of *base Gaussian* and *environment Gaussian* primitives, which is essential for accurate geometry recovery and reflection reconstruction (as demonstrated in Sec. 5.4), our Gaussian tracer must be fully differentiable. This requires computing gradients with respect to the input reflected ray origin, $\frac{d\mathcal{L}}{d\mathbf{o}}$, and direction, $\frac{d\mathcal{L}}{d\mathbf{d}}$. These gradients are backpropagated through the surface position \mathbf{x} and normal \mathbf{n} , obtained during the first rasterization stage, to the *base Gaussian* parameters for joint optimization.

Consider an input ray with origin \mathbf{o} and direction \mathbf{d} , and a intersected triangle primitive i with vertices $\mathbf{v}_1, \mathbf{v}_2, \mathbf{v}_3$. During ray traversal, the OptiX kernel utilizes the GPU’s RT core to determine the intersection depth t_i , which is then

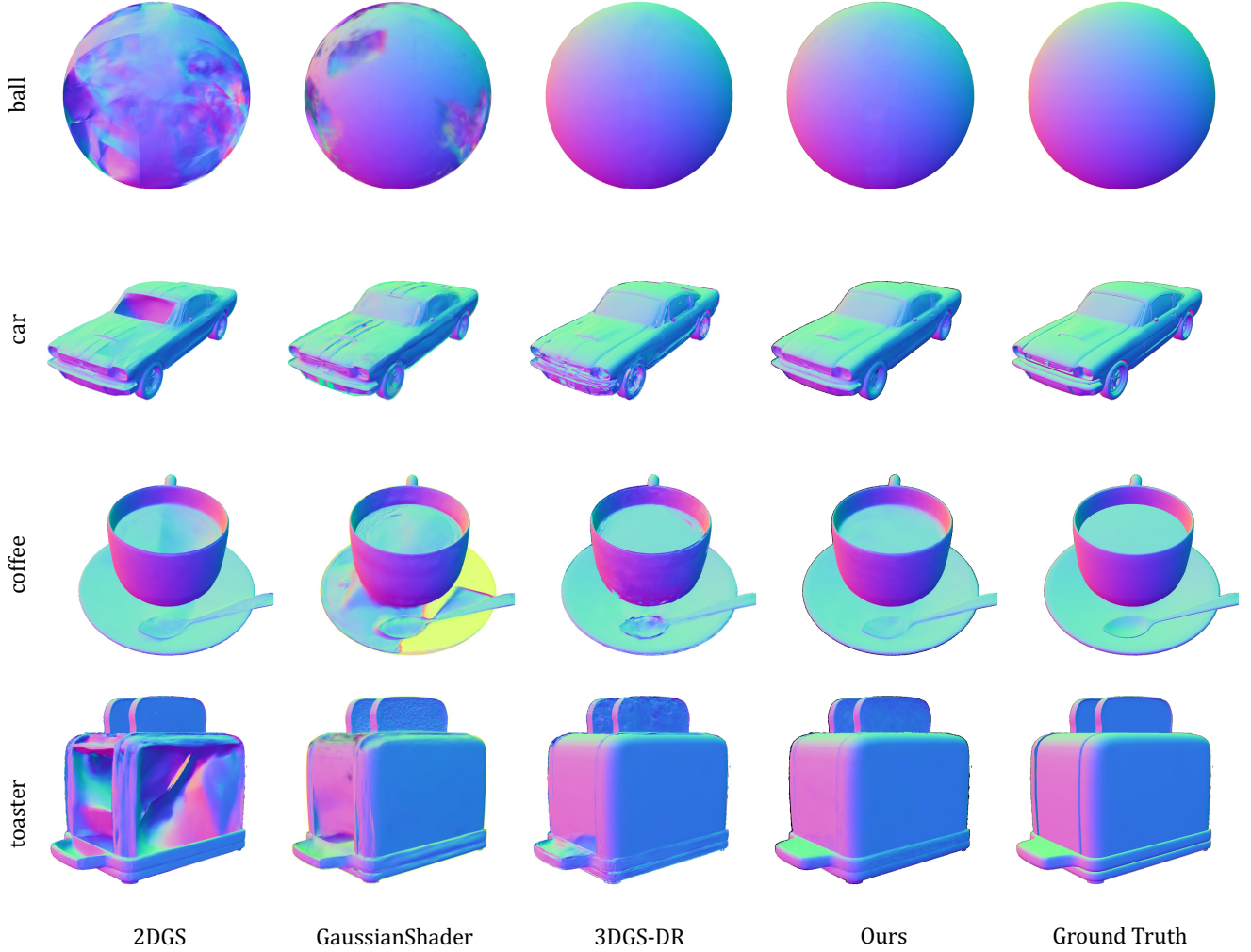


Figure 9. **Qualitative comparisons of normal produced by different methods.**

used to compute the interaction position as $\mathbf{x}_i = \mathbf{o} + t_i \mathbf{d}$. This position is subsequently transformed into the local tangent plane of the corresponding 2D Gaussian, yielding \mathbf{u}_i via Eq. 7 for Gaussian value evaluation. Note that the ray-triangle intersection depth can be manually computed as:

$$t_i = \frac{\mathbf{n}_i^\top (\mathbf{v}_1 - \mathbf{o})}{\mathbf{n}_i^\top \mathbf{d}}, \quad (13)$$

where $\mathbf{n}_i = (\mathbf{v}_2 - \mathbf{v}_1) \times (\mathbf{v}_3 - \mathbf{v}_1)$ is the normal direction of the triangle. Then, we can apply the chain rule to calculate the derivatives w.r.t. the ray origin and direction:

$$\begin{aligned} \frac{d\mathcal{L}}{d\mathbf{o}} &= \frac{d\mathcal{L}}{d\mathbf{x}_i} \frac{d\mathbf{x}_i}{d\mathbf{o}} + \frac{d\mathcal{L}}{dt} \frac{dt}{d\mathbf{o}} \\ &= \frac{d\mathcal{L}}{d\mathbf{x}_i} + \frac{d\mathcal{L}}{dt} \cdot \frac{-\mathbf{n}_i}{\mathbf{n}_i^\top \mathbf{d}}, \end{aligned} \quad (14)$$

and

$$\begin{aligned} \frac{d\mathcal{L}}{d\mathbf{d}} &= \frac{d\mathcal{L}}{d\mathbf{x}_i} \frac{d\mathbf{x}_i}{d\mathbf{d}} + \frac{d\mathcal{L}}{dt} \frac{dt}{d\mathbf{d}} \\ &= \frac{d\mathcal{L}}{d\mathbf{x}_i} \cdot t_i + \frac{d\mathcal{L}}{dt} \cdot \frac{-\mathbf{n}_i^\top (\mathbf{v}_1 - \mathbf{o})}{\mathbf{n}_i \cdot (\mathbf{n}_i^\top \mathbf{d})^2}. \end{aligned} \quad (15)$$

This gradient flow enables the joint optimization of the reflection appearance of *environment Gaussian* alongside the geometry and base appearance of *base Gaussian*, enhancing both geometry accuracy and reflection fidelity.

PSNR \uparrow		Ref-Real [33]			NeRF-Casting Shiny Scenes [34]			
		<i>sedan</i>	<i>toycar</i>	<i>spheres</i>	<i>compact</i>	<i>grinder</i>	<i>hatchback</i>	<i>toaster</i>
Non Real-time	Ref-NeRF* [33]	25.390	22.750	21.120	30.550	33.910	25.210	32.660
	UniSDF [35]	24.680	24.150	22.270	29.720	33.720	27.010	32.900
	ZipNeRF [4]	25.850	23.410	21.770	31.100	34.670	27.780	33.410
	NeRF-Casting [34]	26.770	24.200	23.040	29.730	34.000	27.490	32.870
Real-time	3DGS [15]	25.240	23.910	21.950	28.945	30.885	26.201	29.410
	2DGS [11]	25.065	24.282	22.064	28.415	30.164	25.893	28.630
	GaussianShader [12]	24.081	23.137	21.408	27.474	26.572	24.959	26.641
	3DGS-DR [43]	25.445	23.582	21.539	28.692	30.129	25.985	29.141
	Ours	26.156	24.746	22.949	29.608	33.331	27.220	31.618
SSIM \uparrow		Ref-Real [33]			NeRF-Casting Shiny Scenes [34]			
		<i>sedan</i>	<i>toycar</i>	<i>spheres</i>	<i>compact</i>	<i>grinder</i>	<i>hatchback</i>	<i>toaster</i>
Non Real-time	Ref-NeRF* [33]	0.721	0.612	0.542	0.907	0.880	0.842	0.932
	UniSDF [35]	0.700	0.639	0.567	0.895	0.879	0.845	0.937
	ZipNeRF [4]	0.733	0.626	0.545	0.913	0.887	0.870	0.944
	NeRF-Casting [34]	0.739	0.641	0.597	0.884	0.882	0.853	0.938
Real-time	3DGS [15]	0.713	0.636	0.573	0.877	0.864	0.838	0.928
	2DGS [11]	0.704	0.662	0.595	0.857	0.854	0.819	0.917
	GaussianShader [12]	0.668	0.625	0.573	0.851	0.799	0.805	0.884
	3DGS-DR [43]	0.714	0.635	0.571	0.857	0.849	0.813	0.914
	Ours	0.727	0.667	0.619	0.871	0.895	0.838	0.938
LPIPS \downarrow		Ref-Real [33]			NeRF-Casting Shiny Scenes [34]			
		<i>sedan</i>	<i>toycar</i>	<i>spheres</i>	<i>compact</i>	<i>grinder</i>	<i>hatchback</i>	<i>toaster</i>
Non Real-time	Ref-NeRF* [33]	0.270	0.257	0.257	0.105	0.123	0.156	0.111
	UniSDF [35]	0.309	0.245	0.243	0.122	0.132	0.160	0.107
	ZipNeRF [4]	0.260	0.243	0.238	0.096	0.111	0.130	0.082
	NeRF-Casting [34]	0.254	0.246	0.238	0.148	0.114	0.155	0.096
Real-time	3DGS [15]	0.301	0.237	0.248	0.154	0.181	0.179	0.123
	2DGS [11]	0.344	0.246	0.254	0.193	0.217	0.215	0.147
	GaussianShader [12]	0.371	0.293	0.278	0.189	0.289	0.217	0.169
	3DGS-DR [43]	0.322	0.249	0.251	0.196	0.219	0.228	0.146
	Ours	0.287	0.208	0.229	0.159	0.151	0.177	0.110

Table 5. Ref-Real [33] and NeRF-Casting [34] per-scene breakdowns. All metrics are evaluated at the original resolution downsample by a factor of 4 as prior works [34].

PSNR \uparrow		Shiny Blender Scenes [33]					
		<i>ball</i>	<i>car</i>	<i>coffee</i>	<i>helmet</i>	<i>teapot</i>	<i>toaster</i>
Non Real-time	Ref-NeRF [33]	47.460	30.820	34.210	29.680	47.900	25.700
	UniSDF [35]	44.100	29.860	33.170	38.840	48.760	26.180
	NeRF-Casting [34]	45.460	30.450	33.180	39.100	49.980	26.190
Real-time	3DGS [15]	27.650	27.260	32.300	28.220	45.710	20.990
	2DGS [11]	25.990	26.730	32.360	27.300	44.940	20.272
	GaussianShader [12]	29.081	26.940	31.147	28.883	43.379	23.584
	3DGS-DR [43]	33.533	30.236	34.580	31.518	47.038	26.823
	3iGS [32]	27.640	27.510	32.580	28.210	46.040	22.690
	Ours	32.567	30.598	34.312	31.470	46.582	27.427
SSIM \uparrow		Shiny Blender Scenes [33]					
		<i>ball</i>	<i>car</i>	<i>coffee</i>	<i>helmet</i>	<i>teapot</i>	<i>toaster</i>
Non Real-time	Ref-NeRF [33]	0.995	0.955	0.974	0.958	0.998	0.922
	UniSDF [35]	0.993	0.954	0.973	0.990	0.998	0.945
	NeRF-Casting [34]	0.994	0.964	0.973	0.988	0.999	0.950
Real-time	3DGS [15]	0.937	0.931	0.972	0.951	0.996	0.894
	2DGS [11]	0.935	0.932	0.973	0.952	0.997	0.892
	GaussianShader [12]	0.955	0.930	0.969	0.955	0.996	0.907
	3DGS-DR [43]	0.979	0.957	0.976	0.971	0.997	0.943
	3iGS [32]	0.938	0.930	0.973	0.951	0.997	0.908
	Ours	0.971	0.958	0.974	0.968	0.997	0.945
LPIPS \downarrow		Shiny Blender Scenes [33]					
		<i>ball</i>	<i>car</i>	<i>coffee</i>	<i>helmet</i>	<i>teapot</i>	<i>toaster</i>
Non Real-time	Ref-NeRF [33]	0.059	0.041	0.078	0.075	0.004	0.095
	UniSDF [35]	0.039	0.047	0.078	0.021	0.004	0.072
	NeRF-Casting [34]	0.044	0.033	0.074	0.018	0.002	0.073
Real-time	3DGS [15]	0.162	0.047	0.079	0.081	0.008	0.125
	2DGS [11]	0.155	0.051	0.080	0.080	0.008	0.126
	GaussianShader [12]	0.145	0.066	0.085	0.086	0.011	0.105
	3DGS-DR [43]	0.104	0.038	0.076	0.050	0.006	0.082
	3iGS [32]	0.156	0.045	0.076	0.073	0.006	0.099
	Ours	0.138	0.037	0.085	0.052	0.006	0.077

Table 6. Quantitative results on Shiny Blender Scenes [33].

PSNR \uparrow		Mip-NeRF 360 [3]								
		<i>bicycle</i>	<i>bonsai</i>	<i>counter</i>	<i>flowers</i>	<i>garden</i>	<i>kitchen</i>	<i>room</i>	<i>stump</i>	<i>treehill</i>
Non Real-time	Ref-NeRF* [33]	24.910	32.290	26.020	21.630	27.450	31.610	31.680	25.910	21.790
	UniSDF [35]	24.670	32.860	29.260	21.830	27.460	31.730	31.250	26.390	23.510
	ZipNeRF [4]	25.800	34.460	29.380	22.400	28.200	32.500	32.650	27.550	23.890
	NeRF-Casting [34]	24.920	33.810	28.840	21.750	27.310	32.260	31.660	25.640	23.220
Real-time	3DGS [15]	25.250	31.980	28.700	21.520	27.410	30.320	30.630	26.550	22.490
	2DGS [11]	24.741	31.246	28.107	21.131	26.723	30.372	30.679	26.123	22.427
	GaussianShader [12]	23.103	29.278	26.639	20.267	26.290	27.125	24.098	24.668	20.552
	3DGS-DR [43]	24.869	31.232	27.730	21.116	27.142	28.999	30.068	25.473	21.344
	Ours	25.209	31.946	29.017	21.551	27.709	31.660	31.020	25.423	22.686

SSIM \uparrow		Mip-NeRF 360 [3]								
		<i>bicycle</i>	<i>bonsai</i>	<i>counter</i>	<i>flowers</i>	<i>garden</i>	<i>kitchen</i>	<i>room</i>	<i>stump</i>	<i>treehill</i>
Non Real-time	Ref-NeRF* [33]	0.723	0.935	0.875	0.592	0.845	0.922	0.914	0.731	0.634
	UniSDF [35]	0.737	0.939	0.888	0.606	0.844	0.919	0.914	0.759	0.670
	ZipNeRF [4]	0.769	0.949	0.902	0.642	0.860	0.928	0.925	0.800	0.681
	NeRF-Casting [34]	0.747	0.945	0.887	0.605	0.836	0.924	0.911	0.749	0.653
Real-time	3DGS [15]	0.771	0.938	0.905	0.605	0.868	0.922	0.914	0.775	0.638
	2DGS [11]	0.734	0.931	0.893	0.575	0.844	0.917	0.907	0.756	0.618
	GaussianShader [12]	0.700	0.917	0.875	0.541	0.842	0.888	0.839	0.701	0.579
	3DGS-DR [43]	0.740	0.933	0.889	0.578	0.852	0.908	0.904	0.750	0.607
	Ours	0.734	0.933	0.899	0.589	0.854	0.923	0.910	0.726	0.621

LPIPS \downarrow		Mip-NeRF 360 [3]								
		<i>bicycle</i>	<i>bonsai</i>	<i>counter</i>	<i>flowers</i>	<i>garden</i>	<i>kitchen</i>	<i>room</i>	<i>stump</i>	<i>treehill</i>
Non Real-time	Ref-NeRF* [33]	0.256	0.182	0.213	0.317	0.132	0.121	0.206	0.261	0.294
	UniSDF [35]	0.243	0.184	0.206	0.320	0.136	0.124	0.206	0.242	0.265
	ZipNeRF [4]	0.208	0.173	0.185	0.273	0.118	0.116	0.196	0.193	0.242
	NeRF-Casting [34]	0.231	0.176	0.203	0.312	0.142	0.118	0.216	0.244	0.273
Real-time	3DGS [15]	0.205	0.205	0.204	0.336	0.103	0.129	0.220	0.210	0.317
	2DGS [11]	0.267	0.227	0.229	0.374	0.145	0.146	0.243	0.258	0.374
	GaussianShader [12]	0.275	0.242	0.243	0.380	0.131	0.170	0.307	0.277	0.394
	3DGS-DR [43]	0.254	0.230	0.231	0.368	0.135	0.151	0.247	0.248	0.375
	Ours	0.233	0.180	0.194	0.339	0.112	0.120	0.207	0.262	0.347

Table 7. **Quantitative results on Mip-NeRF 360 [3]**. The results in “Non Real-time” are borrowed from NeRF-Casting [34], and Ref-NeRF* is an improved version of Ref-NeRF [33] that uses Zip-NeRF’s [4] geometry model.